IEEE Open Journal of
Industry Applications

Received 26 May 2023; revised 28 November 2023 and 7 March 2024; accepted 17 March 2024. Date of publication 26 March 2024; date of current version 17 April 2024. The review of this article was arranged by Associate Editor P. Zanchetta.

*Digital Object Identifier 10.1109/OJIA.2024.3381856*

# Noninvasive Measurement of Three-Phase Currents

**PRASAD SHRAWANE (Senior Member, IEEE) AND TARLOCHAN S. SIDHU (Fellow, IEEE)**

Electrical and Computer Engineering Department, Ontario Tech University, Oshawa, Ontario L1G 0C5, Canada

CORRESPONDING AUTHOR: TARLOCHAN SIDHU (e-mail: tarlochan.sidhu@ontariotechu.ca)

**ABSTRACT** This article presents a noninvasive method of measuring three-phase currents using magnetic sensors that can be used for continuous monitoring, automation, and protection of power grids. The nonintrusive nature of these sensors gives operational and economic benefits in installing them at the existing distributed generation sites and power substations. These sensors are linear in operation, free of saturation, and need minimum duration or no outage for installation as compared to the conventional current transformers. This article describes magnetic field simulation, calibration, and experimental validation of magnetic sensors for accurate measurement of three-phase currents. Laboratory experiment results of three-phase low current measurements for two types of overhead structures: triangular and horizontal are rendered as a validation of the proposition. The performance verification of these sensors is further achieved by conducting field experiments for measuring currents up to 1500 A. The sensors yield promising results with a maximum error of 1.15% in the estimation of three-phase currents. The magnetic sensors showed satisfactory performance in accurately reproducing current waveforms consisting of fundamental frequency and harmonics that are typically present in modern power grids.

**INDEX TERMS** Noninvasive sensors, current measurement, magnetic sensors.

## I. INTRODUCTION

The integration of various types of distributed energy resources in combination with inverter-based resources introduced many operating challenges to the reliability, protection, and stability of power systems networks [1], [2], [3]. The interruptions in power delivery are very common and happen for many reasons, such as power system faults due to technical misoperations, extreme weather conditions, equipment failure, planned outages, animals, vehicle accidents, and theft or vandalism [3]. Therefore, the complex network of transmission and distribution lines requires real-time continuous condition monitoring [4]. The records show that the root cause of major disturbances on the bulk power system integrated with solar generators of capacity up to 600 MW is the absence of continuous data monitoring equipment that can monitor high-resolution data of electrical quantities, such as current and voltage, to use for fault isolation. In the absence of adequate data monitoring, faults on the solar or wind power generation stations stay undetected and cause an outage on the feeder of the host utility adding up to the operational cost for utilities [4], [5], [6].

According to the statistics [6], ac overcurrent faults occurred on most inverter-based generation plants because of the inability of the inverters to timely identify current imbalances and misoperate to trip. These faults occurred on medium and high-voltage overhead line networks. Current monitoring devices at various nodes in the grid can be a good solution to resolve this issue. It will help to identify the correct side of the fault on the laterals and block reclosing for underground faults but enabling the reclosing for overhead fault clearing will keep the outage to only specific faulty sections of the feed [7].

Saturation caused by heavy starting fault currents and transient currents is a common problem in current transformers (CTs) that are employed at every existing generation, transmission, and distribution substation. CTs cannot provide accurate estimates of the measured primary current due to saturation. Moreover, the CT saturation with an inductive burden produces a lower distortion index and causes trip delays in protective relays [9]. The time–current characteristics used in a fault-coordinated system can minimize, but not eliminate, possible fault coordination errors because of CT saturation.

In addition, with the increase in the system voltage, the magnitude of current increases, and therefore, the percentage of remanent flux in CTs also increases. It has been observed that 39% of the CTs have 0%–20% of the remanent flux [8], [9]. This signifies that the CTs are more susceptible to saturation if not demagnetized after the fault. It is an expensive procedure to demagnetize the CT if the fault is nonrecurring. This implies that the system needs a complete reset and restart after the fault which increases the outage time, and consequently, the cost of operation. In this scenario, a current measuring device that is free of hysteresis and saturation is easy to install, maintain, and replace at a low cost can be a promising solution.

Magnetic field sensors as an alternative to CTs are getting more attention from researchers. These sensors can measure both static and time-varying magnetic fields unlike CTs. The magnetic sensors chosen for this research are based on the tunneling magnetoresistance effect. A magnetoresistor is a resistor that changes its resistance value in the presence of a magnetic field [10]. The Wheatstone bridge configuration of these sensors allows for both the cancellation of temperature effects (thermal drifts) and a level of immunity to stray magnetic fields. Moreover, in the bridge-type structure, the differential output across the bridge as a function of variation of resistance when applied to a certain magnitude of magnetic field demonstrated good linearity and accuracy of detection [11], [12], [13], [14], [15]. Therefore, it is proven to be efficient and accurate in ac current sensing.

A literature survey on the alternative techniques of current sensing and the use of magnetic sensors in ac current measurement provided thorough information on the present state of their application. A three-phase current measurement based on the array of Hall effect sensors was proposed in [16]. However, the percentage error in the measured currents during the laboratory experiment was up to 15%, and there was no validation of the method provided for field application [16]. The magnetic sensors based on the magnetoresistive effect were proved better in performance compared to Hall effect sensors for ac current measurement by Grandi and Landini [17]. Another study [18] presented an application of a magnetic sensor array for single-phase current measurement up to 500 A. This study did not address the details of the calibration of sensors. Moreover, the sensor array was assembled in a clamp-type structure, which does not support the noninvasive measurement. One team of researchers [19] designed a giant magnetoresistor (GMR) sensor-based clamp for three-phase current measurement and tested its performance on a 10-kV distribution transformer. The experiment gave a promising outcome with sensing of 60 A alternating current. However, there was no result produced for three-phase currents. Another team of researchers [20] employed the TMR sensors for the estimation of fault location in an overhead high-voltage three-phase conductor system by utilizing numerical simulation and suggested a remote monitoring terminal. Recent research on three-phase current measurement for overhead lines presented use of a vertical array of TMR sensors by simulating the 240-kV overhead lines with a decreased ratio of 46.75:1 [21]. The proposed technique in this article achieved three-phase current measurement with a 9.59% error in the estimation of current magnitudes. A comparative study for noninvasive power metering was first explored by using a Hall effect sensor and a TMR sensor [22] for measuring current up to 20 A and proved that TMR sensors can perform better compared to Hall effect sensors. Nonintrusive current sensing was explored by application of copper solenoids in measuring the currents consumed by domestic appliances [23] with an error of 2%–4%. Another research group presented the application of TMR sensors in measuring three-phase currents up to 150 A with good accuracy but faced saturation of the TMR sensor at high currents above thousand amperes [24].

A thorough study of the application of TMR sensors in noninvasively measurement of ac currents demonstrated the effects of various factors on the accuracy of current measurement [25]. This article provides results of the second stage of the research by presenting calibration, testing, and validation of TMR sensors for estimating three-phase fundamental frequency current phasors through laboratory and field experiments with higher accuracy. Section II presents the results of the theoretical simulation of the magnetic field for triangular and horizontal structures for a 15-kV distribution system. Section III describes the details of laboratory experiments including calibration of sensors and validation of sensors for current measurement in triangular and horizontal configurations of the overhead conductors. Section IV describes the field experiment and performance of sensors for three-phase current measurement when the currents are comprised of multiple harmonics. Finally, Section V concludes this article.

## II. MAGNETIC FIELD DUE TO THREE-PHASE CONDUCTORS

The efficacy of measuring magnetic field at a distance for Biot–Savart law can be adopted to determine the magnetic flux intensity $H$ from the magnetic field density $B$ at a distance $d$ from an infinite length conductor carrying a low-frequency current $I$ as

$$B = \mu H = \frac{\mu I}{2\pi d} \text{wb}/\text{m}^2. \tag{1}$$

The study of magnetic fields generated by multiple sources can be performed in detail for three-phase overhead lines with balanced three-phase voltages by adopting (1). A mathematical model is developed for this purpose by considering two types of overhead line arrangements: a triangular arrangement, and a straight-line (horizontal) arrangement for a 15-kV ac power distribution system [26], [27], as shown in Fig. 1(a) and (b). Each phase generates a magnetic field surrounding it because of the time-varying low-frequency balanced sinusoidal voltage source. The resultant magnetic field at any point P1 is a function of the distance from each conductor, time, magnitude, and phase angle of the time-varying current.

If three-phase alternating currents are $I_A(t)$, $I_B(t)$, and $I_C(t)$, then, the magnetic field $B_T$ at point P1 is a function of

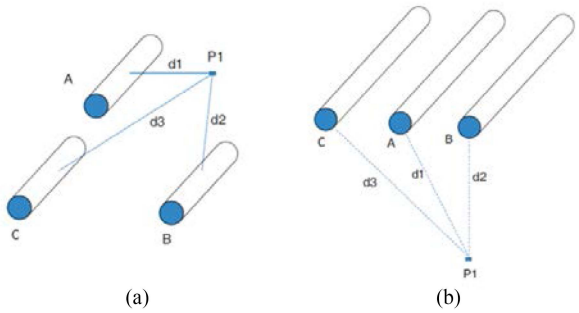


**FIGURE 1.** Magnetic field at point P1 from three phases for (a) triangular structure and (b) horizontal structure.

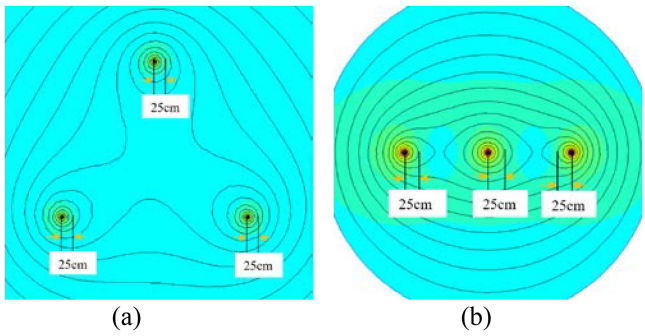


**FIGURE 2.** Magnetic field generated around three phases in (a) triangular structure for 150 A and (b) horizontal structure for 25 A.

combined fields due to all three phases, and can be given as

$$B_T = f\left\{B_A\left(I_A(t), d_1\right), B_B\left(I_B(t), d_2\right), B_C\left(I_C(t), d_3\right)\right\} \quad (2)$$

where $B_A, B_B,$ and $B_C$ are the magnetic field densities produced because of the currents $I_A, I_B,$ and $I_C$ of phase-A, −B, and –C, and $d1, d2,$ and $d3$ are the distances of point P1 from each phase. A balanced three-phase system at a fixed power frequency of 60 Hz is assumed for the generation of three-phase currents.

A preliminary study to verify the relation between distance and magnetic field intensity is performed by developing models in FEMM4.2 software for triangular and horizontal structures and applying 150 A and 25 A currents at 60 Hz. For FEMM modeling, the distances between each phase for both types of structures are referred from the utility standards in the province of Ontario [26], [27].

The resulting magnetic fields are shown in Fig. 2(a) and (b). The circles shown in both these figures indicate the magnetic field intensity and these circles overlap each other indicating the interference of magnetic fields after a certain distance. The current of varying magnitudes from 10 to 150 A was set for both models to study the region of noninterfering fields for each conductor, and it was observed that the appropriate distance in both cases is 25 cm or less for a current from 10 to 150 A for both types of structures. It is inferred from this simulation that the magnetic fields have no interference from the neighboring magnetic fields for points closest to each conductor and can be chosen for estimating individual phase currents from the measured magnetic field. It was observed that for larger currents (>150 A), the distance where no interference will happen would be higher than 25 cm.

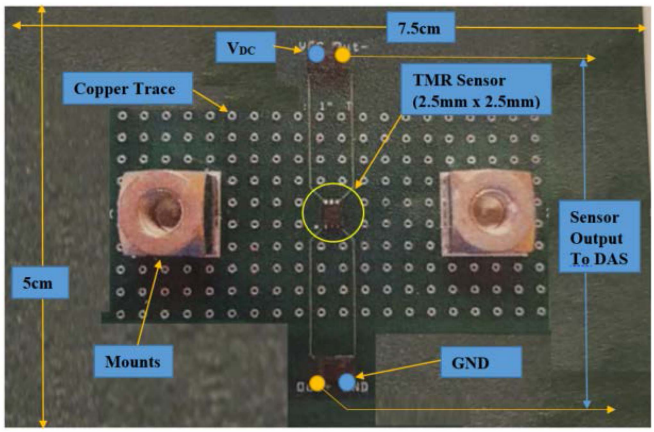


**FIGURE 3.** PCB with TMR sensor.

## III. SENSOR SYSTEM DESIGN

Three high-sensitivity TMR magnetometer sensors of make NVE were selected for the experiment of the three-phase current measurement. These sensors have a bipolar Wheatstone bridge structure for analog output and exhibit very low hysteresis of 1% and with a working temperature range from −50 °C to 125 °C. The sensors are designed for a wide range of frequencies up to 300 kHz. Each sensor is installed on a four-layer PCB with four terminals: two for $V_{DC}$ supply and the other two for analog output. These terminals are connected to respective terminal blocks for connection to AWG#24 wires. PCB has a copper trace with a four-layer structure designed for maximum capability and to minimize the total resistance with temperature rise. The bipolar structure allows the sensor for application of sensing the magnetic fields generated by both direct and alternating currents. The sensor is installed on the PCB of dimension 7.5 cm × 5 cm and, copper trace, mounts, and the terminals for power supply and output are shown in Fig. 3. The mounts are given for providing further mechanical support if needed. However, for this study, the mounting option was not utilized. The copper trace helps as a magnetic field concentrator. The dc power supply is connected across the $V_{DC}$ and GND terminals. The sensor output terminals are connected to the data acquisition system. The installation and application of these sensors in the experimental setup are explained in the next section.

## IV. LABORATORY TESTING

The experiment was carried out using 1-kW resistive circuit per phase. The setup is shown in Fig. 4. A multistranded XLPE aluminum cable of size AWG#4 and three TMR sensors (S1, S2, and S3) were utilized for this experiment. The output of sensors was collected using the I/O connectors and given to the A/D converter for sampling and digitization. A solid-core conventional CT with Class 0.15, 100:100 mA,

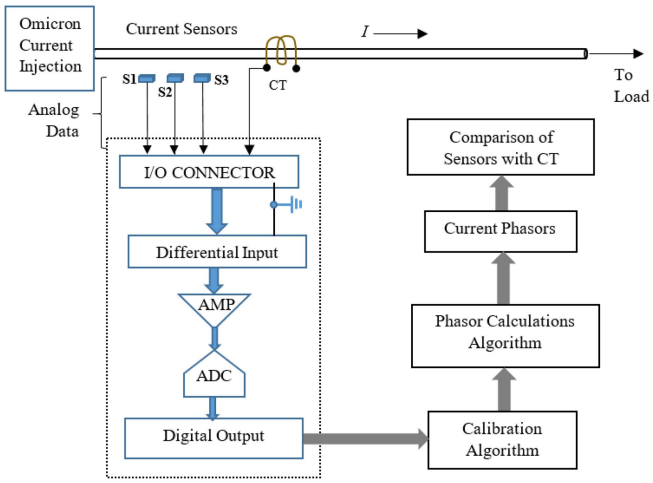


**FIGURE 4.** Laboratory experimental setup.

and 19.7 mm diameter was installed surrounding the cable to compare its performance with the sensors. This CT is Measurement Canada approved and has an exceptionally high accuracy of 0.15% and is mostly used for meter installations. The burden of the CT was designed to meet the IEEE Standard [8]. The TMR sensors operate at 5.5 VDC and their sensitivity is 20 mV/V/mT typical. Omicron CMC356 current injection set was used as the alternating current source for the experiment. The experiment was carried out in three stages. In the first stage, the currents from 5 to 25 A magnitude and 60 Hz frequency were injected in the circuit for cases when the sensors were placed at a right angle from the conductor at distances of 7, 15, 25, and 35 mm. These steps were repeated for two conditions; the first, when the conductor had insulation, and the second, when the conductor had no insulation. The insulation for a length of 40 cm of the same cable was removed to achieve the condition of no insulation.

The outputs of sensors for each case were recorded at a rate of 7.2 kHz by using NI-cDAQ-9174 analog-to-digital converter. In the second stage of the experiment, currents of magnitudes 5–25 A with low frequencies, such as 1, 2, 5, and 10 Hz were injected for cases of all four distances and two conditions of insulation. The corresponding outputs of the CT and three sensors were recorded for each configuration. In this third stage, currents of harmonic frequencies of 2nd, 3rd, 4th, and 5th order with 5–25 A magnitudes were injected into the circuit and corresponding outputs of the sensors and CT for all configurations mentioned earlier were recorded.

The output of the sensors is periodic because of the ac current of a single frequency and, thus, provides 120 samples per cycle for a 60 Hz input current. The collection of samples over one cycle of the signal frequency termed a data window, can be used to estimate the current phasor by applying the nonrecursive discrete Fourier transform (DFT) technique [28]. Subsequent data windows and corresponding phasors are obtained by dropping the oldest sample and adding the newest sample.

**TABLE 1.** Individual and Average Multiplication Factors for Sensors

| S#(A)* | MF for 7 mm | | MF for 15 mm | | MF for 25 mm | | MF for 35 mm | |
|---|---|---|---|---|---|---|---|---|
| | NI* | WI* | NI* | WI* | NI* | WI* | NI* | WI* |
| S1(5) | 678 | 737 | 1155 | 1147 | 1298 | 1932 | 2242 | 2736 |
| S1(10) | 678 | 725 | 1152 | 1159 | 1303 | 1895 | 2336 | 2671 |
| S1(15) | 679 | 731 | 1148 | 1188 | 1302 | 1802 | 2270 | 2561 |
| S1(20) | 677 | 723 | 1142 | 1183 | 1288 | 1790 | 2285 | 2472 |
| S1(25) | 676 | 725 | 1114 | 1178 | 1280 | 1804 | 2258 | 2523 |
| Avg. | 678 | 728 | 1142 | 1171 | 1294 | 1845 | 2278 | 2593 |
| S2(5) | 712 | 906 | 1294 | 1401 | 1895 | 2017 | 2234 | 2535 |
| S2(10) | 717 | 906 | 1308 | 1409 | 1897 | 2015 | 2290 | 2561 |
| S2(15) | 720 | 903 | 1304 | 1400 | 1894 | 2024 | 2233 | 2694 |
| S2(20) | 715 | 902 | 1317 | 1399 | 1876 | 2027 | 2240 | 2589 |
| S2(25) | 719 | 901 | 1317 | 1399 | 1876 | 2018 | 2232 | 2566 |
| Avg. | 717 | 903 | 1308 | 1402 | 1888 | 2021 | 2246 | 2569 |
| S3(5) | 567 | 670 | 819 | 950 | 1361 | 1497 | 1866 | 2116 |
| S3(10) | 564 | 662 | 814 | 956 | 1357 | 1469 | 1902 | 2125 |
| S1(15) | 562 | 663 | 813 | 956 | 1358 | 1453 | 1857 | 2132 |
| S3(20) | 561 | 661 | 810 | 951 | 1361 | 1454 | 1850 | 2111 |
| S3(25) | 560 | 658 | 809 | 948 | 1359 | 1447 | 1855 | 2097 |
| Avg. | 563 | 663 | 813 | 952 | 1359 | 1462 | 1866 | 2116 |

**Note:** S#(A)* denotes Sensor number and current in amperes.

For each sensor, the estimated outputs obtained from the waveforms are converted from rectangular to polar components, and the multiplication factor (MF) (analogous to CT ratio) is calculated from the peak magnitude of the actual injected current of varied magnitudes at 60 Hz and the peak value of the polar magnitude of the estimated current phasor. As a result, each sensor has a separate MF for each range of currents and each distance from the current-carrying conductor. The resulting values of the MFs are shown in Table 1 for all distances for sensors with their variation resulting from inconsistencies in sensor manufacturing.

The measurement errors were calculated between the actual currents and the estimated currents by utilizing individual and average MFs for three sensors for both cases of "No-Insulation (NI)" and "With-Insulation (WI)." Tables 2 and 3 list the average percentage errors in estimated magnitudes for all distances and the selected currents for *NI* and *WI* cases respectively. In both cases, it is observed that the percentage error is below 1.5% when the sensors are placed at 7 mm distance from the conductor.

Moreover, the results in both tables verify that the use of average MFs in current estimation has good performance for currents higher than 5 A for all distances. Therefore, average MFs are utilized for performance verification through laboratory and field experiments presented in the following sections of this article.

### *A. PERFORMANCE AT LOW AND HIGH FREQUENCIES*

The fault currents in power systems comprise lower-order frequencies and affect the current measurement process for

**TABLE 2.** Percent Errors in Estimated Current Magnitude Using Individual and Average MFs: No-Insulation

| S#(A)* | % Errors** for 7 mm | | % Errors** for 15 mm | | % Errors** for 25 mm | | % Errors** for 35 mm | |
|---|---|---|---|---|---|---|---|---|
| | Ind* MF | Avg MF | Ind.* MF | Avg MF | Ind.* MF | Avg MF | Ind.* MF | Avg MF |
| S1(5) | 0.77 | 0.83 | 2.03 | 2.83 | 1.07 | 1.48 | 2.90 | 1.99 |
| S1(10) | 0.14 | 0.24 | 1.13 | 1.69 | 0.27 | 1.00 | 0.89 | 1.23 |
| S1(15) | 0.18 | 0.19 | 0.34 | 0.51 | 0.48 | 0.93 | 0.16 | 0.07 |
| S1(20) | 0.23 | 0.18 | 0.25 | 0.03 | 0.09 | 0.27 | 0.56 | 0.47 |
| S1(25) | 0.07 | 0.15 | 0.31 | 0.14 | 0.33 | 0.73 | 0.35 | 0.96 |
| S2(5) | 0.69 | 0.55 | 0.85 | 0.25 | 1.62 | 2.03 | 4.41 | 3.92 |
| S2(10) | 0.47 | 1.07 | 0.57 | 1.06 | 1.16 | 1.66 | 0.62 | 1.33 |
| S2(15) | 0.35 | 1.41 | 0.17 | 0.35 | 0.68 | 1.03 | 0.74 | 0.18 |
| S2(20) | 0.01 | 0.46 | 0.27 | 1.40 | 0.63 | 0.07 | 0.76 | 0.52 |
| S2(25) | 0.20 | 1.01 | 0.38 | 1.52 | 0.19 | 0.40 | 0.32 | 0.29 |
| S3(5) | 0.76 | 1.45 | 1.03 | 1.76 | 1.66 | 1.82 | 1.27 | 1.27 |
| S3(10) | 0.25 | 0.48 | 0.71 | 1.64 | 0.76 | 0.58 | 0.89 | 1.00 |
| S3(15) | 0.28 | 0.19 | 0.34 | 0.41 | 0.14 | 0.05 | 0.79 | 0.32 |
| S3(20) | 0.04 | 0.28 | 0.05 | 0.05 | 0.43 | 0.54 | 0.26 | 0.59 |
| S3(25) | 0.03 | 0.50 | 0.19 | 0.09 | 0.16 | 0.15 | 0.49 | 0.09 |

*Ind*: Individual*
*%Error** = ((Measured Value-True Value)/True Value)*100*

**TABLE 3.** Percent Errors in Estimated Current Magnitude Using Individual and Average MFs: With-Insulation

| S#(A)* | % Errors** for 7 mm | | % Errors** for 15 mm | | % Errors** for 25 mm | | % Errors** for 35 mm | |
|---|---|---|---|---|---|---|---|---|
| | Ind* MF | Avg MF | Ind.* MF | Avg MF | Ind.* MF | Avg MF | Ind.* MF | Avg MF |
| S1(5) | 0.67 | 1.90 | 0.99 | 1.07 | 1.39 | 3.84 | 2.79 | 5.80 |
| S1(10) | 0.27 | 0.15 | 0.50 | 0.51 | 0.75 | 3.37 | 1.26 | 4.15 |
| S1(15) | 0.11 | 0.54 | 1.07 | 2.47 | 0.32 | 2.05 | 0.97 | 0.29 |
| S1(20) | 0.42 | 0.29 | 0.64 | 1.63 | 1.01 | 2.04 | 0.60 | 4.28 |
| S1(25) | 0.06 | 0.38 | 0.30 | 0.68 | 0.98 | 1.30 | 0.31 | 2.46 |
| S2(5) | 0.84 | 1.48 | 0.75 | 0.72 | 3.73 | 3.55 | 4.72 | 3.43 |
| S2(10) | 0.58 | 0.83 | 0.83 | 1.38 | 1.83 | 1.58 | 2.22 | 1.92 |
| S2(15) | 0.52 | 0.44 | 1.20 | 1.10 | 1.31 | 1.48 | 1.40 | 2.35 |
| S2(20) | 0.22 | 0.06 | 0.69 | 0.52 | 1.48 | 1.84 | 0.94 | 1.69 |
| S2(25) | 0.15 | 0.10 | 0.80 | 0.64 | 1.27 | 1.18 | 0.37 | 0.26 |
| S3(5) | 0.01 | 1.07 | 0.48 | 0.22 | 1.66 | 3.46 | 1.54 | 1.52 |
| S3(10) | 0.15 | 0.03 | 0.40 | 0.77 | 0.75 | 1.21 | 1.18 | 1.60 |
| S3(15) | 0.07 | 0.11 | 0.60 | 1.04 | 0.59 | 0.09 | 0.34 | 1.08 |
| S3(20) | 0.12 | 0.17 | 0.48 | 0.34 | 1.03 | 0.43 | 0.34 | 0.10 |
| S3(25) | 0.20 | 0.50 | 0.40 | 0.02 | 0.55 | 0.51 | 0.18 | 0.73 |

*Ind*: Individual*
*%Error** = ((Measured Value-True Value)/True Value)*100*

CTs due to saturation. In such a scenario, it is crucial to test the performance of sensors. The outputs of all three sensors and CT for 1, 2, 5, and 10 Hz were measured during the second stage of the experiment as explained earlier. The phase angle and magnitude errors were calculated for each sensor and CT to compare their performances. The CT exhibits saturation for lower frequencies and higher currents and therefore results

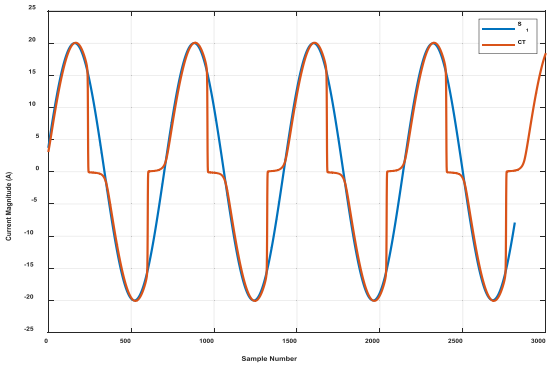


**FIGURE 5.** CT showing saturation and TMR sensor showing accurate output for a current of 20 A at 10 Hz.

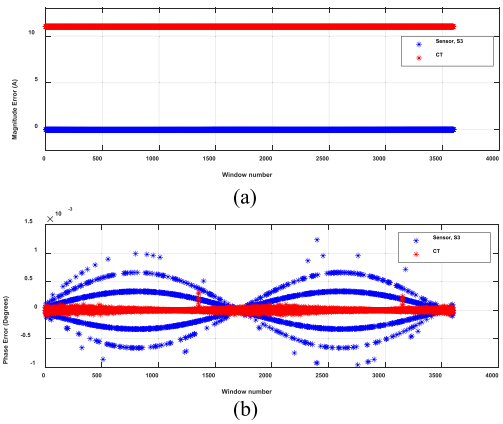


**FIGURE 6.** (a) Magnitude errors and (b) phase angle errors of S3 and CT for 15 A at 2 Hz.

in higher magnitude errors. This is evident from Fig. 5 for a current of 20 A at 10 Hz. Moreover, CT showed high percentage magnitude errors for all currents above 10 A and all low frequencies from 10, 5, 2, and 1 Hz. These high errors indicate rapid and high degree of saturation and therefore, prove nonconformance for measurement of low-frequency currents, whereas all sensors performed consistently for all currents of low frequencies under observation in this experiment. Fig. 5 prominently shows that there is no time lag in the measured samples of the CT and the TMR sensor, with an advantage for TMR sensors showing no saturation. This characteristic behavior of the sensors proves their best suitability in protection and control applications as compared to CTs. Fig. 6(a) shows the comparison of the magnitude of S3 with CT for 15 A current at 2 Hz with a 12.8% error in the magnitude of CT output as compared to a 0.56% error in $S_3$'s estimated output. The phase angle error of CT is low as compared to that of $S_3$ with a minor difference as shown in Fig. 6(b).

Similarly, Fig. 7(a) shows a magnitude error of 18.8% in CT's output at 20 A at 1 Hz, whereas the sensor S1 gave an error of 0.034% for the same current. The angle errors for both CT and S1 are consistently low, but because of the saturation CT exhibits high error, as shown in Fig. 7(b).

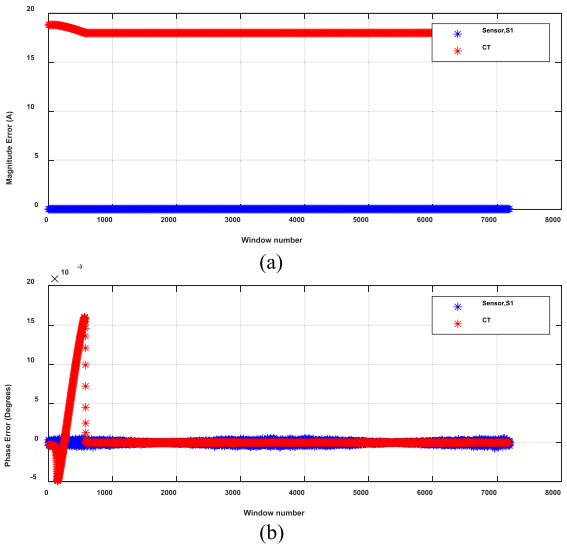


**FIGURE 7.** (a) Magnitude errors and (b) phase angle errors of S1 and CT for 20 A at 1 Hz.

The outputs for various levels of current at even and odd multiples of the fundamental frequency (up to the 5th harmonic) were recorded for the sensor and the CT. It is observed that the magnitude errors for the CT, although small, increase with the increase in the harmonic frequency and magnitude of the input current, whereas the errors are consistently below 1% for all harmonics for the sensor.

### *B. LABORATORY TESTING FOR THREE-PHASE CURRENT MEASUREMENT*

The experimental setup for measuring three-phase currents in the laboratory is shown in Fig. 8(a), whereas the schematic diagram shown in Fig. 8(b) elaborates on the electrical circuit for measuring each phase current using a single sensor placed near the current-carrying conductor. A three-phase resistive circuit is utilized for this experiment with a provision of one sensor for measuring the current of each phase as shown in Fig. 8(b). Two types of structures, i.e., 1) triangular and 2) horizontal type [26], [27], were installed in the laboratory with three-phase resistive loads connected in star-type (Y-type), of which the triangular structure is shown in Fig. 8(a). The sensors are placed on one common side of each phase conductor. Tests were carried out with multiple magnitudes of three-phase source currents from 1 to 15 A injected in the circuit when sensors were placed at 7, 15, 25, and 35 mm.

The magnitude and phase angle errors for each phase were estimated from the measured outputs of three sensors by applying the DFT technique [28] and by comparing their output with the respective source current value of individual phases. The average values of the MFs obtained for each distance were utilized for all required computations in this study. The results were obtained for both types of structures for all distances from the conductor, and are explained in the following sections.

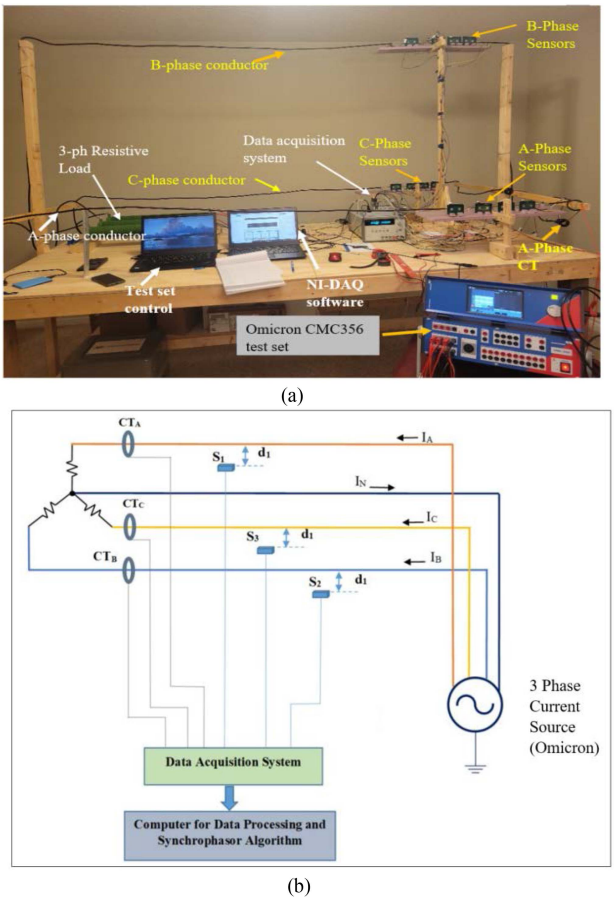


**FIGURE 8.** Three-phase current measurement experimental setup. (a) Laboratory setup. (b) Schematic diagram.

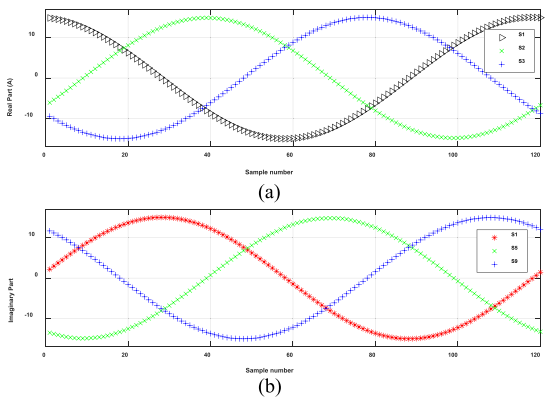


**FIGURE 9.** Estimated output of sensors S1, S2, and S3 placed at 7 mm distance in triangular structure (a) real part and (b) imaginary part for 15 A.

#### 1) TEST RESULTS: TRIANGULAR STRUCTURE

Three sensors, S1, S2, and S3 are used for measuring phase A-phase, B-phase, and C-phase currents, respectively. The real part and the imaginary part of the output current phasors of 15 A obtained for these three sensors are shown in Fig. 9 for the case when the sensors were placed at 7 mm distance from the respective phase conductor. The errors in estimating

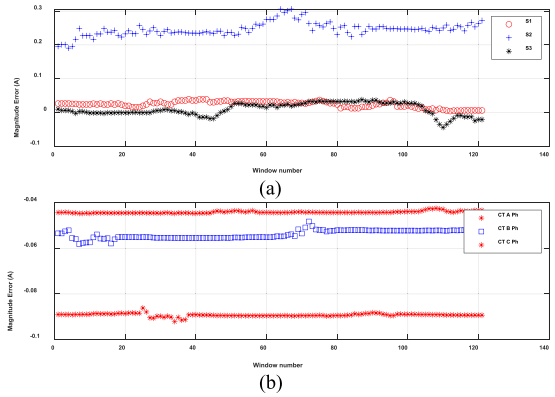


**FIGURE 10.** Magnitude errors in estimated phasors of 15 A for (a) one sensor per phase at 7 mm and (b) three-phase CTs in triangular structure.

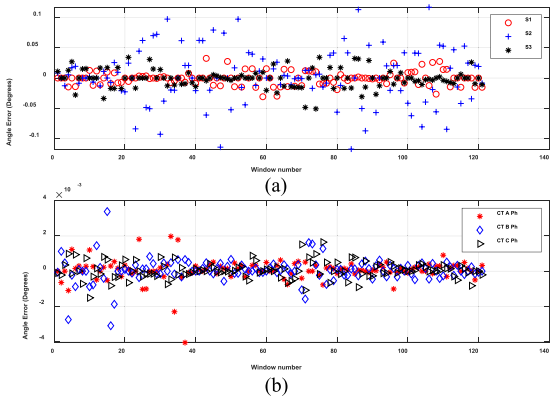


**FIGURE 11.** Angle errors in estimated phasors of 15 A for (a) one sensor per phase at 7 mm and (b) three-phase CTs in triangular structure.

the magnitude for each sample for the 15 A current for these three sensors are shown in Fig. 10(a) with an average variation of 0.013 A for S1, 0.022 A for S2, and 0.020 A for S3. The CTs provided errors of −0.045 A for A-phase CT, −0.058 A for B-phase CT, and −0.087 A for C-phase CT as shown in Fig. 10(b). Similarly, the phase angle errors for the same current were observed to be 0.0001°, 0.00013°, and 0.00014° for S1, S2, and S3 and are shown in Fig. 11(a). The phase angle errors of CTs are shown in Fig. 11(b) indicating smaller errors compared to sensors.

The results of magnitude errors in percentage and the phase angle errors in percentage computed for all sensors for selected distances are given in Table 4.

The performance of sensors for all distances is observed to be consistent for currents up to 15 A for each phase with a magnitude error below 0.004 A with an exception of 0.012 A for 35 mm, as shown in Table 4. The magnitude and phase angle errors are observed to be consistent and satisfactory.

### 2) TEST RESULTS: HORIZONTAL STRUCTURE

The experiment procedure for current injection and measurement of three-phase currents for the horizontal structure is

**TABLE 4.** Performance of Sensors at Various Distances: Triangular Structure

| | Distance of sensors from the conductor of each phase, for Triangular Structure | | | |
|---|---|---|---|---|
| | $d_1 = 7$ mm | $d_2 = 15$ mm | $d_3 = 25$ mm | $d_4 = 35$ mm |
| **Magnitude error, A (average)** | | | | |
| S1-A phase | 0.009 | 0.004 | 0.005 | 0.004 |
| S2-B phase | 0.003 | 0.004 | 0.006 | 0.012 |
| S3-C phase | 0.001 | 0.0002 | 0.007 | 0.005 |
| CT-A phase | 0.054 | 0.064 | 0.063 | 0.065 |
| CT-B phase | 0.035 | 0.035 | 0.034 | 0.035 |
| CT-C phase | 0.036 | 0.035 | 0.036 | 0.037 |
| **Angle error, degrees (average)** | | | | |
| S1-A phase | 0.00015 | 0.0003 | 0.0001 | 0.0002 |
| S2-B phase | 0.00013 | 0.0003 | 0.0001 | 0.0007 |
| S3-C phase | 0.00012 | 0.0001 | 0.0004 | 0.0004 |
| CT-A phase | 0.00001 | 0.00001 | 0.00001 | 0.000007 |
| CT-B phase | 0.00001 | 0.00001 | 0.00001 | 0.000007 |
| CT-C phase | 0.03632 | 0.00001 | 0.00001 | 0.000007 |

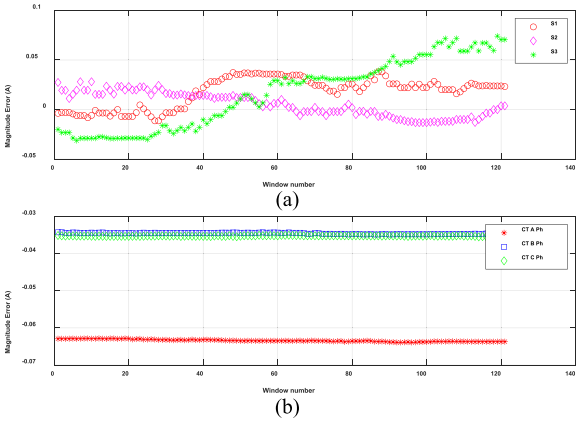


**FIGURE 12.** Magnitude errors in estimated phasors of 10 A for (a) one sensor per phase at 7 mm and (b) three-phase CTs in the horizontal structure.

repeated for the triangular structure. The estimation of performance parameters was done for multiple currents injected using the Omicron CMC356 for the sensors S1, S2, and S3. The magnitude errors for these sensors for 10 A are shown in Fig. 12(a) and for three CTs are shown in Fig. 12(b).

The maximum error in the magnitude for sensor S1 was 0.048 A, 0.039 A for S2, and 0.087 A for S3. The CTs provided minor errors in the magnitude compared to the three sensors. The angle errors for sensors and three CTs are shown in Fig. 13(a) and (b) for 10 A, and a distance of 7 mm. It is observed that the average errors in angles for all sensors are below 0.01°.

The results for sensors and CTs for all distances are provided in Table 5. It is observed from this table that sensor S3 has consistently the lowest magnitude error for all distances as compared to S1 and S2. CTs exhibit higher error as compared to all three sensors. The phase angle errors are minimum for all currents in the case of CTs and for sensors. The performance of sensors was observed to be consistent for all distances with a minor increase in the magnitude error with the increase in the distance.

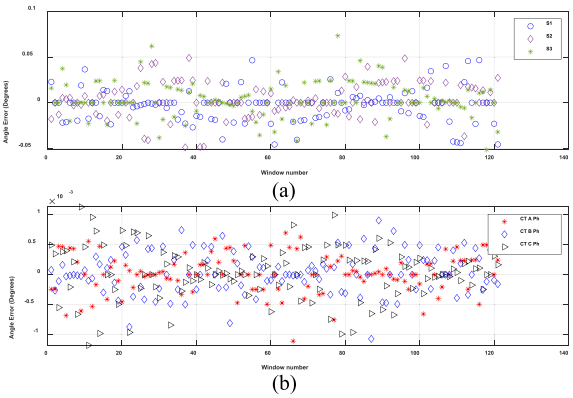


**FIGURE 13.** Angle errors in estimated phasors of 10 A for (a) one sensor per phase at 7 mm and (b) three-phase CTs in the horizontal structure.

**TABLE 5.** Performance of Sensors at Various Distances: Horizontal Structure

| | Distance of sensors from the conductor of each phase, for Horizontal Structure | | | |
|---|---|---|---|---|
| | $d_1$ = 7 mm | $d_2$ = 15 mm | $d_3$ = 25 mm | $d_4$ = 35 mm |
| **Magnitude error, A (average)** | | | | |
| S1-A phase | 0.0002 | 0.003 | 0.007 | 0.005 |
| S2-B phase | 0.002 | 0.003 | 0.008 | 0.007 |
| S3-C phase | 0.001 | 0.001 | 0.006 | 0.011 |
| CT-A phase | 0.063 | 0.644 | 0.064 | 0.064 |
| CT-B phase | 0.034 | 0.357 | 0.034 | 0.034 |
| CT-C phase | 0.036 | 0.033 | 0.033 | 0.033 |
| **Angle error, degrees (average)** | | | | |
| S1-A phase | 0.00006 | -0.00018 | -0.00013 | 0.03705 |
| S2-B phase | 0.00010 | 0.00017 | 0.00027 | 0.00023 |
| S3-C phase | 0.00016 | -0.00002 | 0.00007 | 0.00014 |
| CT-A phase | 0.00001 | 0.00001 | 0.00001 | 0.00001 |
| CT-B phase | 0.00001 | 0.00001 | 0.00001 | 0.00001 |
| CT-C phase | 0.00001 | 0.00001 | 0.00001 | 0.00001 |

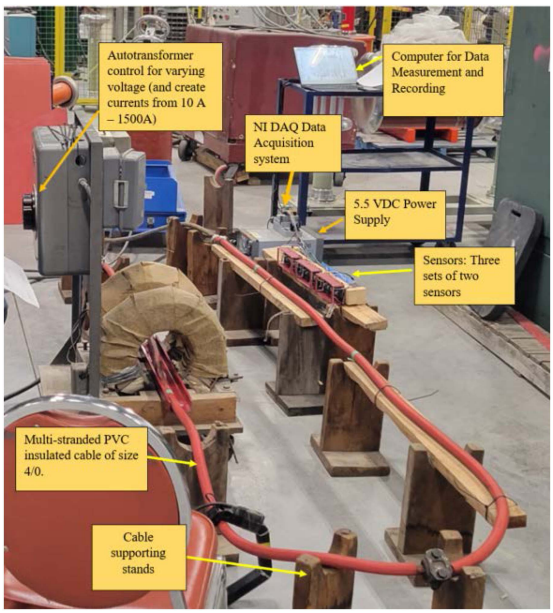


**FIGURE 14.** Experimental setup for measuring high currents.

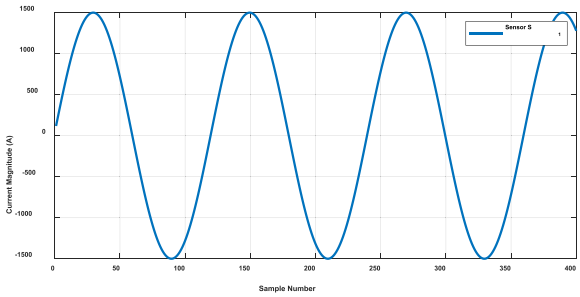


**FIGURE 15.** Sensor S1 output for 1500 A at 15 cm.

### C. LABORATORY TEST RESULTS FOR HIGH CURRENTS

After calibration and verifying the performance of the sensors in the laboratory for currents up to 25 A, the sensors were tested for measuring high currents from 30 to 1500 A in an HV test laboratory. The experimental setup is shown in Fig. 14. Three sensors are placed close to a 4/0 insulated wire such that the distance can be changed for all of them at once. This experimental setup is exactly similar to that shown in Fig. 4 with the exception of the current generating source. In this case, the current source is an autotransformer instead of the Omicron device, and it can generate current from 10 A up to 1500 A.

A high-voltage-rated insulated cable of size 4/0 was utilized for this experiment. Sensors were installed inside a custom-made case made from fiberboard for their protection. The sensors were placed at a distance of 15 cm from the HV cable during the experiment. Currents were varied in steps from 10 to 1500 A and the outputs of three sensors were recorded for 8 s. The data recording device and method were kept the same as in the previous experiment. The magnitude and angle errors from the measured data were estimated for all three sensors using the DFT method mentioned earlier. The estimated output of sensor S1 for an input current of 1500 A at 60 Hz is shown in Fig. 15, which demonstrated high accuracy with a percentage error of 0.1% in the magnitude. The sensors showed no saturation as was the case for the research group [24].

Moreover, this output was estimated from the measured magnetic field at a distance of 15 cm unlike the case in [24] where the sensors were kept touching the cable.

Fig. 16 shows the percentage errors in estimated magnitudes for three sensors for currents from 10 to 1500 A.

It is evident from Fig. 16 that the percentage errors are below 0.8% for all estimated outputs and for all sensors. Fig. 17 shows the box and whisker plot with the percentage errors in phase angles estimated for currents from 10 to 1500 A for all three sensors. The errors in the estimated phase angles for all test currents are observed to be below 0.002% including a few outliers in the estimated outputs for certain currents.

Fig. 18 demonstrates the standard deviation in the estimated magnitudes for all sensors for selected currents from 10 to 1500 A with the highest deviation of 0.58% and average values under 0.4%.

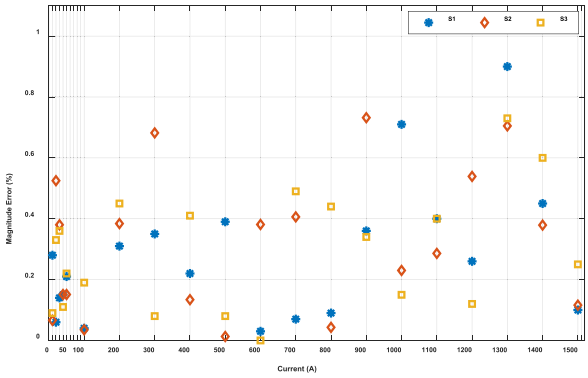


**FIGURE 16.** Magnitude errors for three sensors.

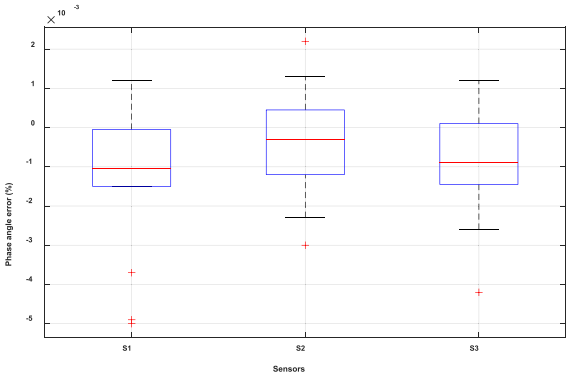


**FIGURE 17.** Percentage errors in phase angle estimation for currents from 10 to 1500 A for S1, S2, and S3.

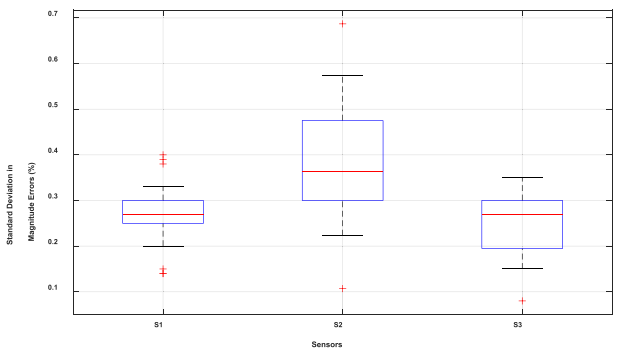


**FIGURE 18.** Standard deviation (%) in magnitude errors obtained for currents from 10 to 1500 A for S1, S2, and S3.

Similarly, Fig. 19 shows the standard deviation in the estimated phase angle errors for all sensors and all test input currents showing consistency in the performance throughout the range of test currents.

## V. FIELD APPLICATION

General Motors Climatic Wind Tunnel (CWT) facility was chosen for field application by installing the sensors on the solar simulation system's three-phase power supply conductors as shown in Fig. 20 and the sensors installed on the AWG#4 insulated conductor per phase are shown in Fig. 21.

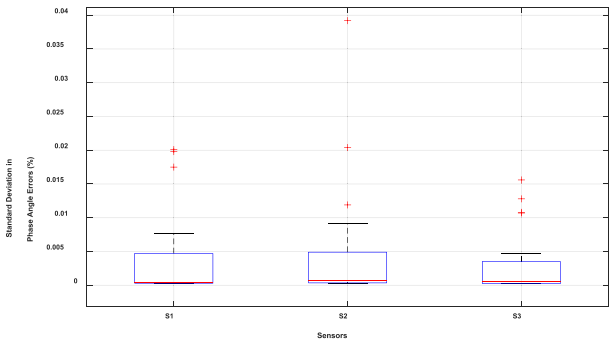


**FIGURE 19.** Standard deviation (%) in angle errors obtained for currents from 10 to 1500 A for S1, S2, and S3.

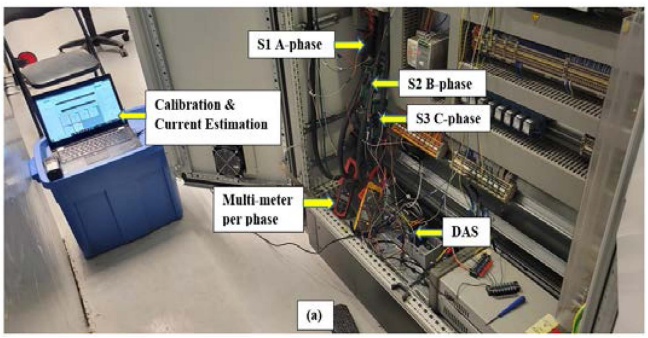


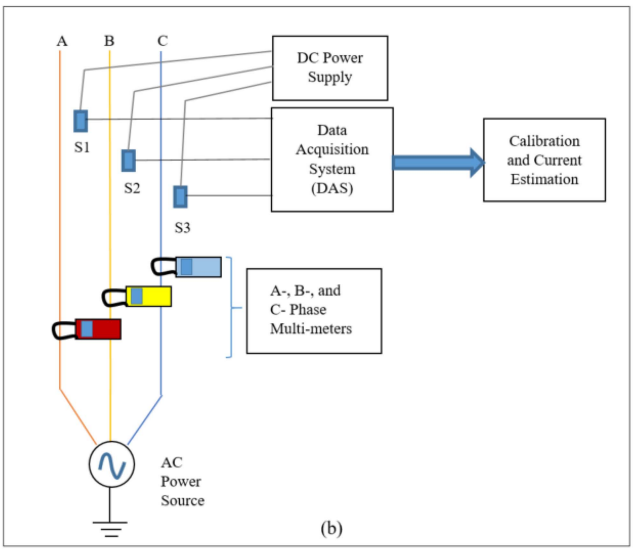


**FIGURE 20.** Three-phase experiment setup at CWT. (a) Actual setup at the facility. (b) Schematic diagram of the circuit.

The experimental setup for three-phase current measurement is elaborated by a schematic diagram shown in Fig. 20(b). The solar simulation system can generate solar intensity from 600 to 1200 kW/m$^2$ from the light produced by metal halide lamps. The ac power distribution panel of this system is supplied by a three-phase 225-kVA delta–star connected transformer with 575 V on the primary and 400/231 V on the secondary side. There were 21 metal halide lamps in the circuit, which are powered by a three-phase source through

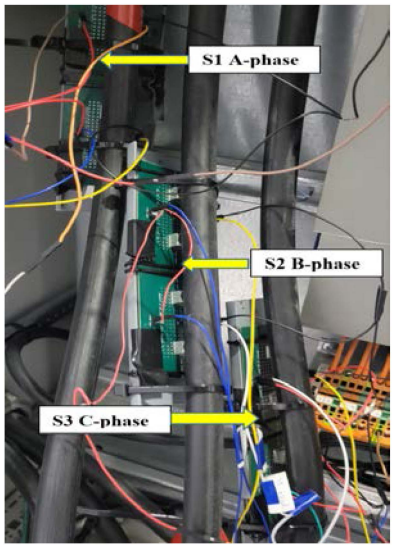


**FIGURE 21.** S1, S2, and S3 installed on A-, B-, and C-phase cables.

this distribution panel. The intensity of all lamps was varied simultaneously by a system of rectifiers and inverters when the ac power was supplied to them. Each lamp also has an electronic ballast. A set of two sensors were installed on each phase inside the distribution panel.

During the experiment, the intensity of all lamps was varied simultaneously from 50% to 100% in stages of 5% by a controller, which was reflected in the increased load current at every stage. The outputs of sensors were recorded at every stage for 5 s. The sampling rate of the data acquisition system was set to 7200 samples/s. For reference, the current flowing in the conductor of each phase for every stage was also measured by using a true rms (TRMS) clamp-on type ammeter, an Etekcity ammeter for A-phase, a FLUKE 325 ammeter for B-phase, and a FLUKE 374 FC ammeter for C-phase. These meters can be seen in Fig. 20(a) and also shown in the schematic diagram in Fig. 20(b). It was observed that phase-A, phase-B, and phase-C loads were not evenly distributed, resulting in unequal currents flowing in each phase and were measured by the ammeters. For example, in one case, A-phase measured 92.6 A, and 113.5 A in B-phase and C-phase, respectively. For B and C phases, the measured currents were 83.9 A for the 50% intensity of lamps and 155.4 A for the 100% intensity. Similarly, for A-phase, the currents were 67.8 A and 130.2 A for 50% and 100% intensity respectively.

### *A. TEST RESULTS*

Three sensors deployed in the field experiment were S1 for A-phase, S2 for B-phase, and S3 for C-phase. A computational program was developed in MATLAB that utilized the multiplying factors and the measured data for each sensor and, estimated the TRMS currents from 120 samples (one cycle of 60 Hz) recorded with a sampling rate of 7200 samples/s for each sensor. The program in MATLAB also estimated

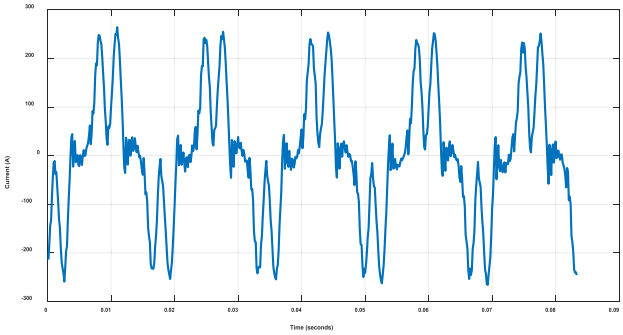


**FIGURE 22.** A-phase current measurement: S1 output at 130.2 A.

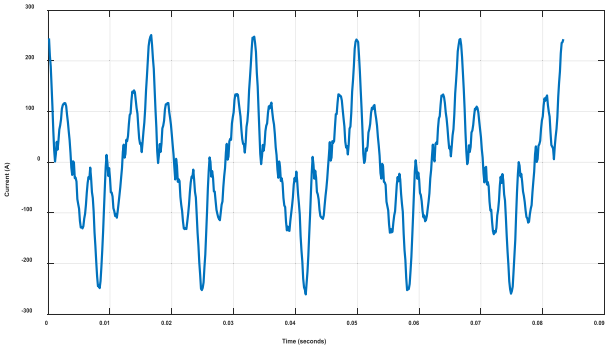


**FIGURE 23.** B-phase current measurement: S2 output for 155.6 A.

the errors in percentage between the TRMS currents obtained from the measured data for sensors and the measured values obtained using clamp-on ammeters for each phase. The estimated output of S1 for 130.2 A of input current is shown in Fig. 22. This figure indicates the presence of multiple harmonics in addition to the fundamental frequency in the load currents. These harmonics are generated because of the gas discharge lamp circuit arcing, negative resistance characteristics, and electronic ballasts with rectifier circuit and inverter.

The results of sensor S1 for measuring A-phase currents for all stages are given in Table 7. The load on this phase consumed currents different than B and C phases. The percentage errors between the ammeter measurements and estimated current outputs vary from 0.22% for 110.8 A to 0.62% for 85.8 A. The sensor showed an error of 0.25% for measuring the input current of 130.2 A.

Fig. 23 shows the output obtained for S2 for an input current of 155.6 A showing a similar pattern in the sine wave with a peak value close to 250 A.

The performance of sensor S2 is illustrated in terms of percentage errors for the B-phase load currents during various stages and is shown in Table 6. This table shows a minimum error of 0.14% in estimating the input current of 91.2 A and a maximum error of 0.83% in estimating the input current of 141.7 A.

The load on B and C phases was balanced and, therefore, provided matching current readings on ammeters for all stages during the experiment as shown in Table 6. The last column of

**TABLE 6. Sensors S1, S2, and S3 Results of Measuring A-Phase, B-Phase, and C-Phase Currents**

| A-Phase sensor S1 | | | B- Phase sensor S2 | | | C- Phase sensor S3 | | |
|---|---|---|---|---|---|---|---|---|
| Rec. Val* | Est. Val.# | *Err.* (%)^ | Rec. Val* | Est. Val.# | *Err.* (%)^ | Rec. Val* | Est. Val.# | *Err.* (%)^ |
| 67.8 | 67.6 | 0.30 | 84.4 | 84.17 | 0.27 | 83.9 | 84.3 | 0.41 |
| 73.4 | 73.6 | 0.26 | 91.2 | 91.07 | 0.14 | 90.6 | 90.3 | 0.32 |
| 79.4 | 78.9 | 0.59 | 98.3 | 97.7 | 0.61 | 97.8 | 97.9 | 0.09 |
| 85.8 | 85.3 | 0.62 | 106.2 | 105.62 | 0.55 | 106.2 | 106.1 | 0.10 |
| 92.1 | 91.84 | 0.29 | 113.6 | 112.99 | 0.54 | 113.6 | 113.6 | 0.00 |
| 98.7 | 98.4 | 0.33 | 121.4 | 120.62 | 0.64 | 121.4 | 121.6 | 0.15 |
| 104.8 | 104.18 | 0.59 | 128.8 | 128.36 | 0.34 | 128.8 | 128.9 | 0.08 |
| 110.8 | 110.55 | 0.22 | 134.8 | 134.56 | 0.18 | 135 | 135.4 | 0.32 |
| 117.2 | 116.53 | 0.57 | 141.7 | 140.52 | 0.83 | 141.6 | 141.8 | 0.16 |
| 123.8 | 123.35 | 0.37 | 148.5 | 147.85 | 0.44 | 148.5 | 149.1 | 0.37 |
| 130.2 | 129.88 | 0.25 | 155.6 | 148.10 | 0.59 | 155.4 | 155.8 | 0.24 |

**Note**: Rec.Val.*: True RMS values recorded from Ammeter in amperes, Est.Val.#: True RMS estimated output values; Err.(%)^: Percentage error between recorded true RMS current and the estimated RMS currents.

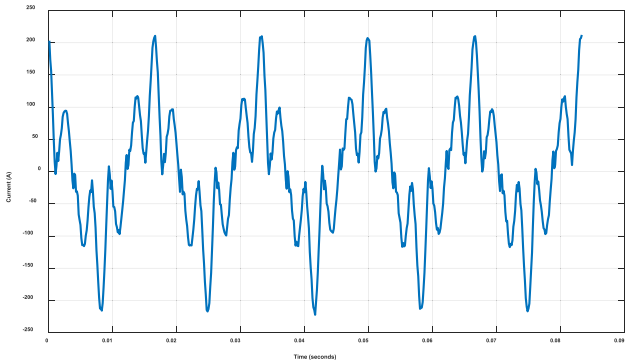


**FIGURE 24. C-phase current measurement: S3 output for 155.6 A.**

this table provides the percentage error between the measured and estimated current at each stage. S3 demonstrated zero error for measuring 113.6 A and a maximum error of 0.37% for measuring 148.5 A. The output of S3 for an input current of 155.4 A is shown in Fig. 24 with its performance similar to that of S2. The waveform shown in Fig. 24 the presence of harmonics introduced by the electronic components in the intensity control circuit of metal halide lamps.

## VI. CONCLUSION

A major objective of the research reported in this article was to demonstrate the application of magnetic sensors for measuring three-phase currents in a nonintrusive manner and without any contact with the current-carrying conductor. Another objective of this research was to showcase the accuracy of measurement using the application of new techniques by deploying magnetic sensors in practical applications. The calibration sensitivity was tested for the cases when the current carrying conductor is insulated and noninsulated with a maximum error of 0.84% and 1.9% for 7 mm distance. The performance of the sensors when installed in three-phase triangular and horizontal structures led to the conclusion that all sensors had magnitude error in the range of 0.002%–0.357% for all distances, and provided better accuracy as compared to CTs. The sensors showed no saturation and consistently high accuracy for all currents up to 1500 A. In addition, the low standard deviation in the magnitude and angle errors for a range of currents from 10 to 1500 A proved that these sensors are accurate in measuring alternating currents for any application.

The sensor system performance was evidently better for measuring low-frequency currents as compared to the conventional CTs, the reason being no saturation of the sensors in contrary to CTs. The magnitude errors of sensors obtained for currents of frequencies from 1 to 10 Hz were very low whereas the CTs showed errors from 8.67% up to 18.8% for the same frequencies. This proved the eligibility of magnetic sensors for measuring fault currents that inherently contain decaying dc offsets characterized by low frequencies.

The field experiment at the CWT facility proved the accuracy and eligibility of sensors in faithfully reproducing three-phase unbalanced currents with harmonics. The overall performance of magnetic sensors for three-phase current measurement supports their suitability as a primary or backup current sensing device for ac circuits in three-phase fault detection and monitoring applications.

## REFERENCES

[1] L. Moslehi and R. Kumar, "A reliability perspective of the smart grid," *IEEE Trans. Smart Grid*, vol. 1, no. 1, pp. 57–64, Jun. 2010.
[2] R. J. Campbell, "Weather-related power outages and electric system resiliency," CRS Report for Congress, Congressional Res. Service, CRS Rep. 7-5700, R42696, pp. 3–14, 2012. [Online]. Available: www.crs.gov
[3] Eaton, "Blackout tracker, Canada annual report 2017," Power Outage Annual Report, Eaton Power Quality Company, Toronto, ON, Canada, 2017. [Online]. Available: https://www.eaton.com/content/dam/eaton/products/backup-power-ups-surge-it-power-distribution/backup-power-ups/blackout-tracker-/eaton-blackout-tracker-annual-report-Canada-2017.pdf
[4] North American Electric Reliability Corporation, "Industry recommendation: Loss of solar resources during transmission disturbances due to inverter settings," North American Electric Reliability Corporation, Atlanta, GA, USA, Jun. 20, 2017, [Online]. Available: https://www.nerc.com/pa/rrm/bpsa/Alerts/NERC_Alert_Loss_of_Solar_Resources_during_Transmission_Disturbance.pdf
[5] North American Electric Reliability Corporation, "Industry recommendation: Loss of solar resources during transmission disturbances due to inverter settings – II," North American Electric Reliability Corporation, Atlanta, GA, USA, May 1, 2018. [Online]. Available: https://www.nerc.com/pa/rrm/bpsa/Alerts/NERC_Alert_Loss_of_Solar_Resources_during_Transmission_Disturbance-II_2018.pdf
[6] North American Electric Reliability Corporation, "Multiple solar PV disturbances in CAISO: Disturbances between June and August 2021; Joint NERC and WECC Staff report," North American Electric Reliability Corporation, Atlanta, GA, USA, Apr. 2022. [Online]. Available: https://www.nerc.com/pa/rrm/ea/Documents/NERC_2021_California_Solar_PV_Disturbances_Report.pdf
[7] "Electrical distribution-system protection," *Cooper Power Syst.*, pp. 27–69, Jan. 2005.
[8] *IEEE Guide for the Application of Current Transformers Used for Protective Relaying Purposes*, IEEE Standard C37.110, 2007.

[9] A. Hargrave, M. Thompson, and B. Heilman, "Beyond the knee point: A practical guide to CT saturation," in *Proc. 71st Annu. Conf. Protective Relay Eng.*, 2018, pp. 1–23.
[10] P. P. Freitas, R. Ferreira, S. Cardoso, and F. Cardoso, "Magnetoresistive sensors," *J. Phys., Condens. Matter*, vol. 19, 2007, Art. no. 165221.
[11] M. Volmer and J. Neamtu, "Micromagnetic analysis and development of high sensitivity spin-valve magnetic sensors," *J. Phys. Conf. Ser.*, vol. 268, 2011, Art. no. 012032.
[12] Z. Li and S. Dixon, "A closed-loop operation to improve GMR sensor accuracy," *IEEE Sens. J.*, vol. 16, no. 15, pp. 6003–6007, Aug. 2016.
[13] G. Grandi and M. Landini, "Magnetic-field transducer based on closed-loop operation of magnetic sensors," *IEEE Trans. Ind. Electron.*, vol. 53, no. 3, pp. 880–885, Jun. 2006.
[14] X. Yang, C. Xie, Y. Wang, W. Yang, and G. Dong, "Optimization design of a giant magnetoresistive effect based current sensor with a magnetic field shielding," *IEEE Trans. Appl. Supercond.*, vol. 24, no. 3, Jun. 2014, Art. no. 9500304.
[15] I. Jedlicska, R. Weiss, and R. Weigel, "Linearizing the output characteristics of GMR current sensors through hysteresis modeling," *IEEE Trans. Ind. Electron.*, vol. 57, no. 5, pp. 1728–1734, May 2010.
[16] G. D'Antona, L. Di Rienzo, R. Ottoboni, and A. Manara, "Processing magnetic sensor array data for ac current measurement in multi-conductor systems," *IEEE Trans. Instrum. Meas.*, vol. 50, no. 5, pp. 1289–1296, Oct. 2001.
[17] G. Grandi and M. Landini, "Magnetic-field transducer based on closed-loop operation of magnetic sensors," *IEEE Trans. Ind. Electron.*, vol. 53, no. 3, Jun. 2006, pp. 880–885.
[18] Y. Chen, Q. Huang, A. H. Khawaja, D. Cai, and J. Wu, "A novel non-invasion magnetic sensor array based measurement of large current," *Measurement*, vol. 139, pp. 78–84, Jun. 2019.
[19] A. D. Xu, L. C. Li, P. Li, Z. M. Wang, Z. B. Wu, and C. J. Hao, "Application of current sensor based on giant magnetoresistance effect in distribution network," *IOP Conf. Ser., Earth Environ. Sci.*, vol. 354, 2019, Art. no. 12058.
[20] Q. Huang, W. Zhen, and P. W. T. Pong, "A novel approach for fault location of overhead transmission line with noncontact magnetic field measurement," *IEEE Trans. Power Del.*, vol. 27, no. 3, pp. 1186–1196, Jul. 2012.
[21] K. Chen, "Intelligent contactless current measurement for overhead transmission lines," *IEEE Trans. Smart Grid*, vol. 13, no. 4, pp. 3028–3037, Jul. 2022.
[22] J. S. Donnal and S. B. Leeb, "Noncontact power meter," *IEEE Sensors J.*, vol. 15, no. 2, pp. 1161–1169, Feb. 2015.
[23] P. Pai, L. Chen, F. K. Chowdhury, and M. Tabib-Azar, "Non-intrusive electric power sensors for smart grid," in *Proc. IEEE Sensors*, 2012, pp. 1–4.
[24] P. Li et al., "A contactless current sensor based on TMR chips," *IEEE Trans. Instrum. Meas.*, vol. 71, 2022, Art. no. 9511711.
[25] P. Shrawane and T. S. Sidhu, "Performance of a noninvasive magnetic sensor-based current measurement system in power systems," *Electronics*, vol. 10, 2021, Art. no. 2869.
[26] Utility Standards Forum, "Overhead primary framing," USF Section Jan. 1–17, 2017, 2017.
[27] Utility Standards Forum, "Voltages, line locations and clearances for distribution circuits," USF Section Apr. 2, 2017, 2017.
[28] A. G. Phadke and J. S. Thorp, "Phasor estimation of nominal frequency inputs," in *Computer Relaying for Power Systems*, 2nd ed. Hoboken, NJ, USA: Wiley, Aug. 2009, ch. 2, pp. 29–48.

**PRASAD SHRAWANE** (Senior Member, IEEE) received the Ph.D. degree in electrical and computer engineering from the Department of Electrical and Computer Engineering, Ontario Tech University, Oshawa, ON, Canada, in 2023.

He is a Registered Professional Engineer in the province of Ontario and is working in the power industry with a focus on protection and control.

**TARLOCHAN S. SIDHU** (Fellow, IEEE) received the Ph.D. degree in electrical engineering from the University of Saskatchewan, Saskatoon, Canada, in 1989.

He is currently a Professor with the Department of Electrical and Computer Engineering, Ontario Tech University, Oshawa, ON, Canada. From 2012 to 2020, he was the Dean of the Faculty of Engineering and Applied Science with Ontario Tech University. Before this, he was the Chair of the Department of Electrical and Computer Engineering at the University of Western University and also held Senior Industrial Research Chair.